Stability-Guaranteed Impedance Control of Hydraulic Robotic Manipulators

Janne Koivumäki and Jouni Mattila, *Member, IEEE*

Abstract—In challenging robotic tasks, high-bandwidth closed-loop control performance of the system is required for successful task completion. One of the most critical factors inhibiting the wide-spread use of closed-loop contact control applications has been the control system stability problems. To prevent unstable system behavior, the need for rigorously addressed manipulator dynamics is substantial. This is because the contact dynamics between a manipulator and its environment can be drastic.

In this paper, a novel Cartesian space impedance control method is proposed for hydraulic robotic manipulators. To address the highly nonlinear dynamic behaviour of the hydraulic manipulator, the system control is designed according to the subsystem-dynamics-based virtual decomposition control (VDC) approach. The unique features of VDC (*virtual power flow and virtual stability*) are used to analyze the interaction dynamics between the manipulator and the environment. Based on the desired impedance parameters and stability analysis, an explicit method to design the control gains for the proposed impedance control law is developed. The L_2 and L_∞ stability is guaranteed in both free-space motions and constrained motions.

Experimental results demonstrate that the hydraulic robotic manipulator is capable of adjusting its dynamic behaviour accurately in relation to the imposed target impedance behaviour. This provides compliant system behaviour, which is needed in many dynamically challenging robotic tasks.

Index Terms—hydraulic manipulators, impedance control, nonlinear model-based control, stability analysis, virtual decomposition control, virtual power flow.

I. Introduction

ADVANCED robotic systems, such as humanoid robots, legged robots and exoskeletons, are currently receiving substantial attention in industry and academia. From a mechanical design perspective, hydraulic actuators provide an attractive solution for robotic systems because they can produce significant forces/torques for their size, are robust and can provide accurate motions. Indeed, hydraulic robotic systems, such as Boston Dynamics' BigDog, Cheetah and Atlas, and SARCOS' humanoids and exoskeletons, have already advanced the state-of-the-art in robotics. Academic in-depth research is also ongoing (e.g., IIT's HyQ and Shandong University's SCalf). For robotic systems, articulated limbs are crucially important subsystems because they can provide many versatile abilities, such as legged locomotion or manipulation of the environment. However, successful completion of these interactive tasks requires that the robotic system is capable of accurately controlling its interaction with the surrounding environment, with humans or with other devices.

However, force control of a single hydraulic actuator is challenging due to its highly nonlinear dynamic behaviour [1]. Moreover, control design for articulated robotic systems is greatly complicated by the nonlinear nature of the associated multibody dynamics. Impeded by these nonlinearities, an accurate contact control for articulated hydraulic robots becomes an extremely challenging task. In robotic contact control, system stability issues have drawn considerable attention since the installation of the first industrial robots, and numerous reasons for the unstable responses have been identified [2]–[6]. One reason is that contact dynamics between the robotic system and the environment can be drastic while robot nonlinear dynamics are not considered rigorously [4], [7].

The design challenges mentioned above have led to the utilization of nonlinear model-based control (NMBC) methods to achieve better dynamic performance for hydraulic robots, which is needed in dynamically challenging contact tasks. In contrast to linear control methods, NMBC methods (where the specific feedforward control term can be used for system nonlinearities) can theoretically provide "infinite" control bandwidth, as long as proper feedforward control is designed [8]. As introduced in many books on the control of robots, such as [9]–[11], typical NMBC designs are based on the complete dynamic models of robots using the Lagrangian formulation. However, for complex robots (such as humanoids), the implementation of complete-dynamics-based control becomes substantially challenging, because with these methods, the complexity (computational burden) of robot dynamics is proportional to the fourth power of the number of degrees of freedom (DOF) in motion [8].

Virtual decomposition control (VDC) [8], [12] is a unique subsystem-dynamics-based control method using the Newton-Euler formulation. A number of significant state-of-the-art control performance improvements have been reported with VDC with electrically-driven robots (see [13]–[18]) and with hydraulically-driven robots (see [19]–[23]). The subsystem-dynamics-based control of the VDC enables NMBC design with many attractive special features for (complex) robotic systems, including the following: 1) control computations are proportional to the number of subsystems and can be performed even by locally embedded hardware/software, 2) subsystem dynamics remain relatively simple with fixed dynamic structures invariant to the target system, 3) changing the control (or dynamics) of one subsystem does not affect the control equations within the rest of the system, 4) parameter uncertainties in the subsystem dynamics can be addressed with a parameter adaptation and 5) system stability analysis can be

addressed at a subsystem level using the unique features of VDC, *virtual power flow* (VPF) and *virtual stability*.

In this paper, a novel non-switching impedance control method is proposed. To address the highly nonlinear dynamic behavior of the hydraulic manipulator and to obtain the rigorous dynamic performance needed in contact control tasks, the manipulator's internal control is designed based on VDC. Interaction dynamics between the manipulator and the environment are analyzed using a VPF located at the contact point. Based on the analysis, an interconnection between the desired impedance parameters (characterizing system target impedance behaviour) and the parameters of the proposed novel impedance control method can be found such that impedance behavior can be designed for the system.

This paper provides the following contributions. 1) A novel non-switching impedance control method, including the VDC design and the proposed Cartesian space impedance control laws, is developed for hydraulic manipulators. 2) The impedance control is designed using the framework of VDC. 3) A rigorous stability proof for a hydraulic manipulator is provided for the first time to cover both free-space motions and constrained motions. 4) The experiments demonstrate the efficiency of the proposed method and rigorously support the mathematical theorems on the stability-guaranteed system behaviour and the target impedance behaviour.

This paper is organized as follows. Section II describes contact control strategies proposed for hydraulic robotic systems. Section III introduces the essential mathematical foundations needed in system control design. Section IV describes the proposed impedance control design and its VDC-based implementation. Section V concentrates on system stability issues. Section VI demonstrates contact control performance of the proposed controller. Conclusions are outlined in Section VII.

II. RELATED WORKS

The basic approaches for robotic force control are based on hybrid position/force control by Raibert [24] and impedance control by Hogan [25]. Historical overviews of robot force control can be found in [7], [26], [27]. With electrically-driven manipulators, the force control, as presented, e.g., in [24], [25], [28]–[32], has been extensively studied. Typically, hydraulic manipulators are built to operate heavy objects (e.g., logs) or to exert large forces on the physical environment (e.g., in excavation). Thus, it is rather surprising that only a few studies exist regarding force control in hydraulic robotic manipulators.

Heinrich et al. [33] implemented the impedance control technique for hydraulically-actuated manipulators for the first time. A nonlinear proportional-integral (NPI) controller was developed for joint control. The stability proof of the proposed controller design was not given.

Tafazoli et al. [34] (see also related studies in [35], [36]) studied the impedance control of a teleoperated mini-excavator, based on a simple proportional-derivative (PD) controller. Stability proof for a simple PD impedance controller was provided, but it was limited to a single-DOF hydraulic cylinder acting on the environment.

Zeng and Sepehri [37] proposed a nonlinear tracking control for multiple hydraulic manipulators handling a rigid object,

where internal forces of coupled manipulators were controlled. The control design for the system was based on a backstepping methodology and the stability of the system was proven. However, the stability analysis was limited to situations where connection to the held object was already established. The experiments were carried out with two single-axis electro-hydraulic actuators, which were connected rigidly to the common object with spring mechanisms [38], preventing unilateral constraint.

Semini et al. [39] reported their recent results on the active impedance control of hydraulic quadruped robot HyQ. They used input-output feedback linearization to construct their model-based control design for the hydraulic leg. Rigorous stability proof for their control design was not provided.

A major step forward from the existing solutions was taken by Koivumäki and Mattila [23], who proposed a stability-guaranteed contact force/motion control for heavy-duty hydraulic manipulators. In this study, the highly nonlinear behaviour of the hydraulic manipulator was addressed with the VDC approach, and hybrid motion/force control was used to control end-effector motions and forces in their own subspaces. In the experiments, superior motion and force tracking performance were reported. In the control design, switching from free-space motion to constrained motion was utilized.

In summary, NMBC for hydraulic manipulators with non-switching contact control law and with rigorous stability proof in free-space and constrained motions is still an open problem. This problem is addressed in the present paper.

III. MATHEMATICAL FOUNDATION

This section provides essential mathematical foundations needed in control system design.

A. Linear/Angular Velocity Vectors and Force/Moment Vectors

Consider an orthogonal, three-dimensional coordinate system {$\mathbf{A}$} (called frame {$\mathbf{A}$} for simplicity) attached to the rigid body. Let the linear/angular velocity vector of frame {$\mathbf{A}$} be written as ${}^{\mathbf{A}}V = [{}^{\mathbf{A}}\mathbf{v} \ {}^{\mathbf{A}}\omega]^T$, where ${}^{\mathbf{A}}\mathbf{v} \in \mathbb{R}^3$ and ${}^{\mathbf{A}}\omega \in \mathbb{R}^3$ are the linear and angular velocity vectors of frame {$\mathbf{A}$}. Similarly, let the force/moment vector in frame {$\mathbf{A}$} be written as ${}^{\mathbf{A}}F = [{}^{\mathbf{A}}\mathbf{f} \ {}^{\mathbf{A}}\mathbf{m}]^T$, where ${}^{\mathbf{A}}\mathbf{f} \in \mathbb{R}^3$ and ${}^{\mathbf{A}}\mathbf{m} \in \mathbb{R}^3$ are the force and moment vectors applied to the origin of frame {$\mathbf{A}$}, expressed in frame {$\mathbf{A}$}. Then, consider two given frames, denoted as {$\mathbf{A}$} and {$\mathbf{B}$}, fixed to a common rigid body. The following relations hold

$$ {}^{\mathbf{B}}V = {}^{\mathbf{A}}\mathbf{U}_{\mathbf{B}}^{T}{}^{\mathbf{A}}V \tag{1} $$

$$ {}^{\mathbf{A}}F = {}^{\mathbf{A}}\mathbf{U}_{\mathbf{B}}{}^{\mathbf{B}}F \tag{2} $$

where ${}^{\mathbf{A}}\mathbf{U}_{\mathbf{B}} \in \mathbb{R}^{6 \times 6}$ denotes a force/moment transformation matrix that transforms the force/moment vector measured and expressed in frame {$\mathbf{B}$} to the same force/moment vector measured and expressed in frame {$\mathbf{A}$}.

B. Parameter Adaptation

The following projection function from [8] is used for parameter adaptation:

Definition 1: A projection function $\mathscr{P}(s(t), k, a(t), b(t), t) \in \mathbb{R}$ is a differentiable scalar function defined for $t \geqslant 0$ such that its time derivative is governed by

$$\dot{\mathscr{P}} = k s(t) \kappa \qquad (3)$$

with

$$\kappa = \begin{cases} 0, & \text{if } \mathscr{P} \leqslant a(t) \text{ and } s(t) \leqslant 0 \\ 0, & \text{if } \mathscr{P} \geqslant b(t) \text{ and } s(t) \geqslant 0 \\ 1, & \text{otherwise} \end{cases}$$

where $s(t) \in \mathbb{R}$ is a scalar variable, $k > 0$ is a constant and $a(t) \leqslant b(t)$ holds.

The projection function defined in (3) has the following property: For any constant $\mathscr{P}_c$ subject to $a(t) \leqslant \mathscr{P}_c \leqslant b(t)$, it follows that

$$(\mathscr{P}_c - \mathscr{P})\left(s(t) - \frac{1}{k}\dot{\mathscr{P}}\right) \leqslant 0. \qquad (4)$$

C. Virtual Cutting Points and a Simple Oriented Graph

In the VDC approach, the original system is virtually decomposed into the subsystems by placing conceptual *virtual cutting points* (VCPs). A *cutting point* forms a virtual cutting surface on which three-dimensional force vectors and three-dimensional moment vectors can be exerted from one part to another. The VCP is defined as shown in Definition 2.

Definition 2 [8]: A cutting point is a directed separation interface that conceptually cuts through a rigid body. At the cutting point, two parts resulting from the virtual cut maintain equal positions and orientations. The cutting point is interpreted as a *driving cutting point* by one part and is simultaneously interpreted as a *driven cutting point* by another part. A force vector $\mathbf{f} \in \mathbb{R}^3$ and a moment vector $\mathbf{m} \in \mathbb{R}^3$ are exerted from one part to which the cutting point is interpreted as a *driving cutting point* to the other part to which the cutting point is interpreted as a *driven cutting point*.

After the original system is virtually decomposed into subsystems by placing VCPs, the system can be represented by a simple oriented graph. A simple oriented graph is defined, as shown in Definition 3.

Definition 3 [8]: A graph consists of nodes and edges. A directed graph is a graph in which all edges have directions. An oriented graph is a directed graph in which each edge has a unique direction. A simple oriented graph is an oriented graph in which no loop is formed.

D. L_2 and L_∞ Stability

Definition 4 [8]: Lebesgue space, denoted as L_p with p being a positive integer, contains all Lebesgue measurable and integrable functions $f(t)$ subject to

$$\|f\|_p = \lim_{T \to \infty} \left[\int_0^T |f(t)|^p d\tau\right]^{\frac{1}{p}} < +\infty. \qquad (5)$$

Two particular cases are considered:
(a)   A Lebesgue measurable function $f(t)$ belongs to L_2 if and only if $\lim_{T \to \infty} \int_0^T |f(t)|^2 d\tau < +\infty$.
(b)   A Lebesgue measurable function $f(t)$ belongs to L_∞ if and only if $\max_{t \in [0,\infty)} |f(t)| < +\infty$.

The following Lemma 1 (Lemma 2.3 in [8]) provides that a system is stable with its affiliated vector $\mathbf{x}(t)$ being a function in L_∞ and its affiliated vector $\mathbf{y}(t)$ being a function in L_2.

Lemma 1 [8]: Consider a non-negative differentiable function $\xi(t)$ defined as

$$\xi(t) \geqslant \frac{1}{2}\mathbf{x}(t)^T \mathbf{P}\mathbf{x}(t) \qquad (6)$$

with $\mathbf{x}(t) \in \mathbb{R}^n$, $n \geqslant 1$ and $\mathbf{P} \in \mathbb{R}^{n \times n}$ being a symmetric positive-definite matrix. If the time derivative of $\xi(t)$ is Lebesgue integrable and governed by

$$\dot{\xi}(t) \leqslant -\mathbf{y}(t)^T \mathbf{Q}\mathbf{y}(t) - s(t) \qquad (7)$$

where $\mathbf{y}(t) \in \mathbb{R}^m$, $m \geqslant 1$ and $\mathbf{Q} \in \mathbb{R}^{m \times m}$ being a symmetric positive-definite matrix and $s(t)$ is subject to

$$\int_0^\infty s(t)dt \geqslant -\gamma_0 \qquad (8)$$

with $0 \leqslant \gamma_0 < \infty$, then it follows that $\xi(t) \in L_\infty$, $\mathbf{x}(t) \in L_\infty$ and $\mathbf{y}(t) \in L_2$ hold.

The following Lemma 2 provides that L_2 and L_∞ signal retains its properties after passing through a first-order multiple-input-multiple-output (MIMO) filter.

Lemma 2 [8]: Consider a first-order MIMO system described by

$$\dot{\mathbf{x}}(t) + \mathbf{K}\mathbf{x}(t) = \mathbf{u}(t) \qquad (9)$$

with $\mathbf{x}(t) \in \mathbb{R}^n$, $\mathbf{u}(t) \in \mathbb{R}^n$, and $\mathbf{K} \in \mathbb{R}^{n \times n}$ being symmetrical and positive-definite. If $\mathbf{u}(t) \in L_2 \bigcap L_\infty$ holds, then $\mathbf{x}(t) \in L_2 \bigcap L_\infty$ and $\dot{\mathbf{x}}(t) \in L_2 \bigcap L_\infty$ hold.

The following Lemma 3 provides an asymptotic convergence for an error signal $e(t)$.

Lemma 3 [40]: If $e(t) \in L_2$ and $\dot{e}(t) \in L_\infty$, then $\lim_{t \to \infty} e(t) = 0$.

E. Virtual Stability

The unique feature of the VDC approach is the introduction of a scalar term, namely the *virtual power flow* (VPF); see Definition 5. VPFs uniquely define the dynamic interactions among the subsystems and play an important role in the definition of *virtual stability*, which is defined in Definition 6.

Definition 5 [8]: The VPF with respect to frame $\{\mathbf{A}\}$ can be defined as the inner product of the linear/angular velocity vector error and the force/moment vector error as

$$p_{\mathbf{A}} = (^{\mathbf{A}}V_r - {}^{\mathbf{A}}V)^T (^{\mathbf{A}}F_r - {}^{\mathbf{A}}F) \qquad (10)$$

where $^{\mathbf{A}}V_r \in \mathbb{R}^6$ and $^{\mathbf{A}}F_r \in \mathbb{R}^6$ represent the required vectors of $^{\mathbf{A}}V \in \mathbb{R}^6$ and $^{\mathbf{A}}F \in \mathbb{R}^6$, respectively.

Definition 6 [8]: A subsystem with a driven VCP to which frame $\{\mathbf{A}\}$ is attached and a driving VCP to which frame $\{\mathbf{C}\}$ is attached is said to be *virtually stable* with its affiliated vector $\mathbf{x}(t)$ being a virtual function in L_∞ and its affiliated vector $\mathbf{y}(t)$ being a virtual function in L_2, if and only if there exists a non-negative accompanying function

$$\nu(t) \geqslant \frac{1}{2}\mathbf{x}(t)^T \mathbf{P}\mathbf{x}(t) \qquad (11)$$

such that

$$\dot{\nu}(t) \leqslant -\mathbf{y}(t)^T \mathbf{Q}\mathbf{y}(t) + p_{\mathbf{A}} - p_{\mathbf{C}} - s(t) \qquad (12)$$
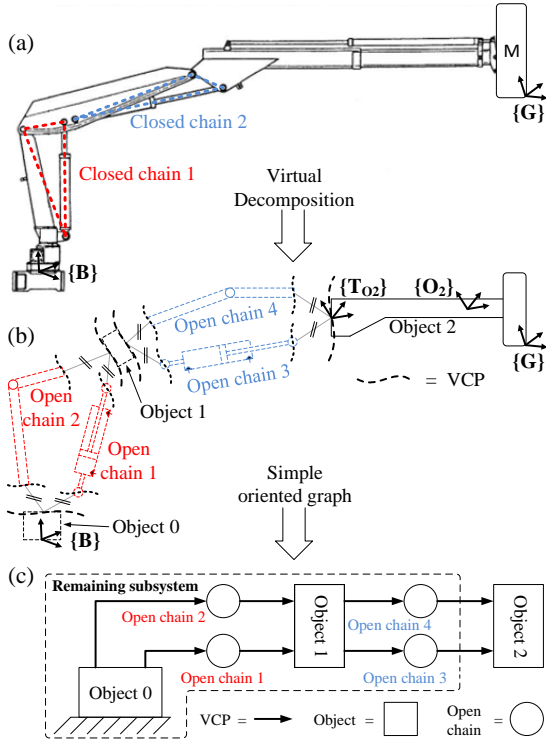
Fig. 1. The studied system. Subfigure (a) shows the original two-DOF hydraulic manipulator. Subfigure (b) shows a virtual decomposition of the system. Note the parallelism (//) in the VCPs. Subfigure (c) shows a simple oriented graph of the virtually decomposed system.

holds, subject to

$$\int_0^\infty s(t)dt \geqslant -\gamma_s \tag{13}$$

with $0 \leqslant \gamma_s < \infty$, where $\mathbf{P}$ and $\mathbf{Q}$ are two block-diagonal positive-definite matrices and p_A and p_C denote the VPFs (by Definition 5) at frames $\{\mathbf{A}\}$ and $\{\mathbf{C}\}$, respectively.

IV. CONTROL OF THE MANIPULATOR

This section addresses a design of novel impedance control method for a two-DOF hydraulic manipulator, which is shown in Fig. 1(a). Even though a two-DOF system is studied in this paper, the developed approach is extendable to systems with any number of actuators. First, to address the highly nonlinear behaviour of the hydraulic manipulator, Section IV-A shows the manipulator's internal control design based on the VDC approach. Then, Section IV-B introduces the novel impedance control method, designed using the framework of VDC.

A. Virtual Decomposition Control

The first step in the VDC approach is to virtually decompose an original system into subsystems (i.e., *objects* and *open chains*) by placing conceptual VCPs (see Definition 2). Then, the decomposed subsystems are represented by a simple oriented graph imposing dynamic interactions among subsystems. The system's virtual decomposition and the simple oriented graph presentation are addressed in Section IV-A1.

Then, the subsystem-dynamic-based control is designed to make each subsystem qualified to be *virtually stable*. The virtue of the VDC is that when all subsystems are virtually stable, the stability of the entire system can be guaranteed. This is addressed in Section V.
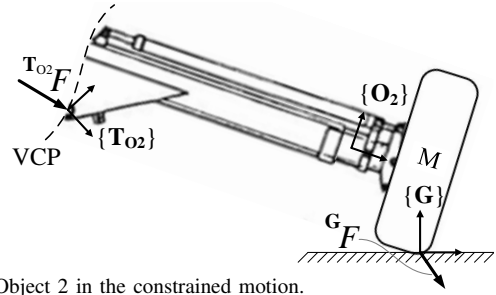

Fig. 2. Object 2 in the constrained motion.

1) Virtual Decomposition and Simple Oriented Graph: The virtually decomposed manipulator is shown in Fig. 1(b). As discussed, changing the control (or dynamics) of one subsystem does not affect the control equations within the rest of the system. In this study, only the control equations subject to Object 2 have been changed in relation to [23]. For this reason, only the control design for Object 2 (subsystem interacting with the environment) has been studied in detail in this paper. Control designs for the remaining subsystems, shown at the dashed line in Fig. 1(b), can be found in [23].

The simple oriented graph for the manipulator is shown in Fig. 1(c). In this paper, the subsystems inside the dashed line in Fig. 1(c) are considered as one subsystem; see the corresponding lines in Fig. 1(b). Each subsystem corresponds to a node, and each VCP corresponds to a directed edge whose direction defines the force reference direction. Thus, a VCP is simultaneously interpreted as a driving VCP by one subsystem (from which the force/moment vector is exerted or the directed edge is pointing away) and as a driven VCP by another subsystem (toward which the force/moment vector is exerted or the directed edge points) [8].

Next, in Sections IV-A2 through IV-A4, the kinematics, dynamics and control of Object 2 are given.

2) Object 2 – Kinematics: Fig. 2 shows the Object 2, to which frame $\{\mathbf{O_2}\}$ is fixed to describe the force and motion specifications. Frame $\{\mathbf{T_{O2}}\}$ exists at the driven VCP of Object 2, and frame $\{\mathbf{G}\}$ is the end-effector target frame where the contact occurs and in which the Cartesian motion and force control is specified.

The linear/angular velocity vector $^{\mathbf{G}}V \in \mathbb{R}^6$ in frame $\{\mathbf{G}\}$ can be written as

$$^{\mathbf{G}}V = \mathbf{N_c}\dot{\boldsymbol{\chi}} \tag{14}$$

where $\dot{\boldsymbol{\chi}} \in \mathbb{R}^2$ is the Cartesian velocity vector and the mapping matrix $\mathbf{N_c}$ can be written as

$$\mathbf{N_c} = \begin{bmatrix} 1 & 0 & 0 & 0 & 0 & 0 \\ 0 & 1 & 0 & 0 & 0 & 0 \end{bmatrix}^T.$$

The following relations hold for Object 2:

$$\begin{aligned} ^{\mathbf{O_2}}V &= {}^{\mathbf{G}}\mathbf{U}_{\mathbf{O_2}}^T \, {}^{\mathbf{G}}V \\ &= {}^{\mathbf{T_{O2}}}\mathbf{U}_{\mathbf{O_2}}^T \, {}^{\mathbf{T_{O2}}}V. \end{aligned} \tag{15}$$

3) Object 2 – Dynamics: The end-effector force/moment vector in frame $\{\mathbf{G}\}$ can be written as

$$^{\mathbf{G}}F = \mathbf{N_c}\,{}^{\mathbf{G}}f \tag{16}$$

where $^{\mathbf{G}}f \in \mathbb{R}^2$ is a Cartesian contact force vector (exerted by the manipulator on the environment).

The net force/moment vector ${}^{\mathbf{O_2}}F^* \in \mathbb{R}^6$ of Object 2, expressed in frame $\{\mathbf{O_2}\}$, can be written in view of [8] as

$$\mathbf{M_{O_2}}\frac{d}{dt}({}^{\mathbf{O_2}}V) + \mathbf{C_{O_2}}({}^{\mathbf{O_2}}\omega){}^{\mathbf{O_2}}V + \mathbf{G_{O_2}} = {}^{\mathbf{O_2}}F^* \quad (17)$$

where $\mathbf{M_{O_2}} \in \mathbb{R}^{6\times6}$ denotes the mass matrix, $\mathbf{C_{O_2}}({}^{\mathbf{O_2}}\omega) \in \mathbb{R}^{6\times6}$ denotes the matrix of Coriolis and centrifugal terms and $\mathbf{G_{O_2}} \in \mathbb{R}^6$ denotes the gravity terms.

On the other hand, the net force/moment vector (i.e., force resultant equation) for Object 2 can be written as

$$ {}^{\mathbf{O_2}}F^* = {}^{\mathbf{O_2}}\mathbf{U_{T_{o2}}}{}^{\mathbf{T_{o2}}}F - {}^{\mathbf{O_2}}\mathbf{U_G}{}^{\mathbf{G}}F. \quad (18)$$

4) Object 2 – Control: This section addresses the VDC-based rigid body control of Object 2.

Similar to (14), the required linear/angular velocity vector in the end-effector target frame $\{\mathbf{G}\}$ can be written as

$$ {}^{\mathbf{G}}V_{\mathrm{r}} = \mathbf{N_c}\dot{\boldsymbol{\chi}}_{\mathrm{r}} \quad (19)$$

where $\dot{\boldsymbol{\chi}}_{\mathrm{r}} \in \mathbb{R}^2$ is the required Cartesian space velocity (design) vector specified later in (31).

In view of (15), the required velocity transformations in Object 2 can be written as

$$\begin{aligned} {}^{\mathbf{O_2}}V_{\mathrm{r}} &= {}^{\mathbf{G}}\mathbf{U}_{\mathbf{O_2}}^T {}^{\mathbf{G}}V_{\mathrm{r}} \\ &= {}^{\mathbf{T_{o2}}}\mathbf{U}_{\mathbf{O_2}}^T {}^{\mathbf{T_{o2}}}V_{\mathrm{r}}. \end{aligned} \quad (20)$$

Similar to (16), the required force/moment vector in the end-effector target frame $\{\mathbf{G}\}$ can be obtained as

$$ {}^{\mathbf{G}}F_{\mathrm{r}} = \mathbf{N_c}{}^{\mathbf{G}}\boldsymbol{f}_{\mathrm{d}} \quad (21)$$

where ${}^{\mathbf{G}}\boldsymbol{f}_{\mathrm{d}} \in \mathbb{R}^2$ is a desired Cartesian contact force vector.

Then, in view of [8], the required net force/moment vector for Object 2 can be written as

$$ {}^{\mathbf{O_2}}F_{\mathrm{r}}^* = \mathbf{Y_{O_2}}\widehat{\boldsymbol{\theta}}_{\mathbf{O_2}} + \mathbf{K_{O_2}}({}^{\mathbf{O_2}}V_{\mathrm{r}} - {}^{\mathbf{O_2}}V) \quad (22)$$

with

$$\mathbf{Y_{O_2}}\boldsymbol{\theta}_{\mathbf{O_2}} = \mathbf{M_{O_2}}\frac{d}{dt}({}^{\mathbf{O_2}}V_{\mathrm{r}}) + \mathbf{C_{O_2}}({}^{\mathbf{O_2}}\omega){}^{\mathbf{O_2}}V_{\mathrm{r}} + \mathbf{G_{O_2}} \quad (23)$$

where regressor matrix $\mathbf{Y_{O_2}} \in \mathbb{R}^{6\times13}$ and parameter vector $\boldsymbol{\theta}_{\mathbf{O_2}} \in \mathbb{R}^{13}$ can be solved as shown in [8, in Appendix A]. Moreover, in (22), $\widehat{\boldsymbol{\theta}}_{\mathbf{O_2}}$ denotes the estimate of $\boldsymbol{\theta}_{\mathbf{O_2}}$ and $\mathbf{K_{O_2}}$ is a symmetric positive-definite matrix characterizing the velocity feedback control.

The estimated parameter vector $\widehat{\boldsymbol{\theta}}_{\mathbf{O_2}}$ in (22) needs to be updated. Define

$$\mathbf{s_{O_2}} = \mathbf{Y}_{\mathbf{O_2}}^T({}^{\mathbf{O_2}}V_{\mathrm{r}} - {}^{\mathbf{O_2}}V). \quad (24)$$

Then, (3) can be used to update the ith element of $\widehat{\boldsymbol{\theta}}_{\mathbf{O_2}}$ as

$$\widehat{\theta}_{\mathbf{O_2}i} = \mathscr{P}(s_{\mathbf{O_2}i}, \rho_{\mathbf{O_2}i}, \underline{\theta}_{\mathbf{O_2}i}, \overline{\theta}_{\mathbf{O_2}i}, t), \forall i \in \{1,2,...,13\} \quad (25)$$

where $\widehat{\theta}_{\mathbf{O_2}i}$ denotes the ith element of $\widehat{\boldsymbol{\theta}}_{\mathbf{O_2}}$, $s_{\mathbf{O_2}i}$ denotes the ith element of $\mathbf{s_{O_2}}$, $\rho_{\mathbf{O_2}i} > 0$ is the update gain, and $\underline{\theta}_{\mathbf{O_2}i}$ and $\overline{\theta}_{\mathbf{O_2}i}$ denote the lower bound and the upper bound of $\theta_{\mathbf{O_2}i}$.

In relation to (18), the required force resultant equation can be written as

$$ {}^{\mathbf{O_2}}F_{\mathrm{r}}^* = {}^{\mathbf{O_2}}\mathbf{U_{T_{o2}}}{}^{\mathbf{T_{o2}}}F_{\mathrm{r}} - {}^{\mathbf{O_2}}\mathbf{U_G}{}^{\mathbf{G}}F_{\mathrm{r}}. \quad (26)$$

Finally, the following Lemma 4 is used to prove the *virtual stability* of Object 2.

Lemma 4: Consider Object 2, described by (15), (17) and (18), combined with its control equations (20), (22) and (26) and with the parameter adaptation (24) and (25). Let the non-negative accompanying function $v_{\mathbf{O_2}}$ be

$$\begin{aligned} v_{\mathbf{O_2}} = &\frac{1}{2}({}^{\mathbf{O_2}}V_{\mathrm{r}} - {}^{\mathbf{O_2}}V)^T\mathbf{M_{O_2}}({}^{\mathbf{O_2}}V_{\mathrm{r}} - {}^{\mathbf{O_2}}V) \\ &+ \frac{1}{2}\sum_{i=1}^{13}\frac{(\theta_{\mathbf{O_2}i} - \widehat{\theta}_{\mathbf{O_2}i})^2}{\rho_{\mathbf{O_2}i}} \end{aligned} \quad (27)$$

Then, the time derivative of (27) can be expressed by

$$\dot{v}_{\mathbf{O_2}} \leqslant -({}^{\mathbf{O_2}}V_{\mathrm{r}} - {}^{\mathbf{O_2}}V)^T\mathbf{K_{O_2}}({}^{\mathbf{O_2}}V_{\mathrm{r}} - {}^{\mathbf{O_2}}V) + p_{\mathbf{T_{O2}}} - p_{\mathbf{G}} \quad (28)$$

where $p_{\mathbf{T_{O2}}}$ is the VPF by Definition 5 at the driven VCP of Object 2, and $p_{\mathbf{G}}$ characterizes the VPF between the end-effector and the environment.

Proof: The proof is similar to Appendix B in [23]. ∎

Remark 1: Note that Object 2 has only one VCP (see Fig. 2) but two VPFs exists in (28). The VPF $p_{\mathbf{T_{O2}}}$ locates at the VCP in Object 2. Thus, for the *virtual stability* of Object 2, a solution (which satisfies Definition 6) must be found for the VPF $p_{\mathbf{G}}$ in (28). This will be addressed later in Section V-A.

B. The Design of the Proposed Impedance Control

In this section, the impedance control law by Hogan [25] is introduced first in Section IV-B1. Then, the proposed Cartesian space impedance control laws are designed in Section IV-B2.

1) Impedance Control Law: In view of Hogan [25], the target impedance for the manipulator can be described as

$$ {}^{\mathbf{G}}\boldsymbol{f}_{\mathrm{d}} - {}^{\mathbf{G}}\boldsymbol{f} = -\mathbf{M_d}(\ddot{\boldsymbol{\chi}}_{\mathrm{d}} - \ddot{\boldsymbol{\chi}}) - \mathbf{D_d}(\dot{\boldsymbol{\chi}}_{\mathrm{d}} - \dot{\boldsymbol{\chi}}) - \mathbf{K_d}(\boldsymbol{\chi}_{\mathrm{d}} - \boldsymbol{\chi}) \quad (29)$$

where $\mathbf{M_d} \in \mathbb{R}^{2\times2}$, $\mathbf{D_d} \in \mathbb{R}^{2\times2}$ and $\mathbf{K_d} \in \mathbb{R}^{2\times2}$ are diagonal positive-definite matrices and characterize the desired inertia, damping and stiffness, respectively. Neglecting the inertia term in (29), the target impedance can be written as

$$ {}^{\mathbf{G}}\boldsymbol{f}_{\mathrm{d}} - {}^{\mathbf{G}}\boldsymbol{f} = -\mathbf{D_d}(\dot{\boldsymbol{\chi}}_{\mathrm{d}} - \dot{\boldsymbol{\chi}}) - \mathbf{K_d}(\boldsymbol{\chi}_{\mathrm{d}} - \boldsymbol{\chi}). \quad (30)$$

Then, the following Assumption 1 is made for the desired impedance parameters $\mathbf{D_d}$ and $\mathbf{K_d}$.

Assumption 1: The desired damping $\mathbf{D_d}$ and stiffness $\mathbf{K_d}$ are selected such that: 1) their ratio and magnitudes are not subject to unstable behavior in the overall system; and 2) the target impedance in (30) is attainable for the manipulator.

Assumption 1 imposes the condition that the impedance parameters $\mathbf{D_d}$ and $\mathbf{K_d}$ must be selected within the dynamic range of achievable impedance, so-called Z-width [41], which defines the combination of stiffness and damping that can be passively achieved by a certain mechanism. One method to define Z-width for hydraulic articulated systems is given in [42].

2) Proposed Impedance Control Laws: In the framework of VDC, the required velocity[1] serves as a reference trajectory for a system and the control objective is to make the controlled actual velocities track the required velocities. In this section, the

---

[1] The general format of a required velocity includes a desired velocity (which usually serves as a reference trajectory for a system) and one or more terms that are related to control errors [8].
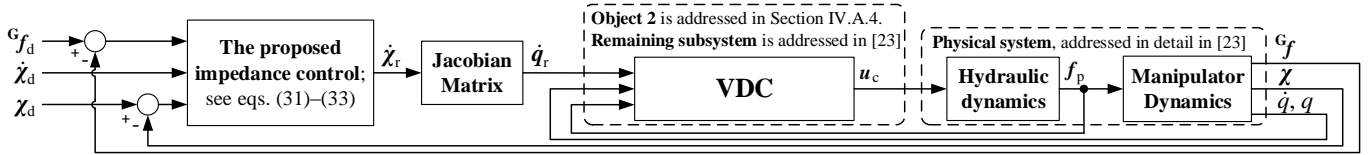
Fig. 3. Diagram of the designed novel impedance control for the hydraulic manipulator. The required Cartesian velocity $\dot{\boldsymbol{\chi}}_r$ is computed from (31). Then, the required joint velocity vector $\dot{\boldsymbol{q}}_r$ is solved using the Jacobian matrix. The detailed structure for the remaining subsystem (see Fig. 1) inside the VDC block can be found in [23]. The output $\boldsymbol{u}_c$ of the VDC block is the control signal for the hydraulic valves, which control the hydraulic cylinders. Finally, the motion dynamics of the manipulator is produced by the output force $\boldsymbol{f}_p$ of the hydraulic cylinders. Please see [23] for more details.

objective is to design such a control for the required Cartesian velocity vector $\dot{\boldsymbol{\chi}}_r \in \mathbb{R}^2$ in (19), which 1) realizes the Cartesian impedance behaviour for the manipulator and 2) qualifies Object 2 as *virtually stable* in the sense of Definition 6.

Let $\dot{\boldsymbol{\chi}}_r$ for the manipulator be designed as

$$\dot{\boldsymbol{\chi}}_r = \dot{\boldsymbol{\chi}}_d + \boldsymbol{\Lambda}_\chi(\boldsymbol{\chi}_d - \boldsymbol{\chi}) + \boldsymbol{\Lambda}_f({}^G\boldsymbol{f}_d - {}^G\boldsymbol{f}) \quad (31)$$

where $\boldsymbol{\Lambda}_\chi \in \mathbb{R}^{2\times 2}$ and $\boldsymbol{\Lambda}_f \in \mathbb{R}^{2\times 2}$ are two diagonal positive-definite matrices characterizing Cartesian position and force control, and let them be defined according to Condition 1.

Condition 1: The diagonal positive-definite matrices $\boldsymbol{\Lambda}_f$ and $\boldsymbol{\Lambda}_\chi$ are defined as

$$\boldsymbol{\Lambda}_f = \mathbf{D}_d^{-1} \quad (32)$$
$$\boldsymbol{\Lambda}_\chi = \mathbf{K}_d\mathbf{D}_d^{-1}. \quad (33)$$

Then, the following Theorem 1 provides that the target impedance behaviour (30) can be achieved for the system.

Theorem 1: Consider the proposed control law (31), which defines the required velocity behaviour for the system. If and only if the diagonal positive-definite matrices $\boldsymbol{\Lambda}_f$ and $\boldsymbol{\Lambda}_\chi$ in (31) are defined according to (32) and (33) in Condition 1, then the control law (31) equals the target impedance law (30).

Proof: See Appendix A. ∎

A diagram for the proposed control design is shown in Fig. 3.

Remark 2: Compared to the typical Cartesian free-space control law, term $\boldsymbol{\Lambda}_f({}^G\boldsymbol{f}_d - {}^G\boldsymbol{f})$ is included in (31). In this study, ${}^G\boldsymbol{f}_d = [0\ 0]^T$ is used. This enables a high control bandwidth in free space (see free-space results in [22]), provided that zero contact force is measured in free-space motions, i.e., $({}^G\boldsymbol{f}_d - {}^G\boldsymbol{f}) = \mathbf{0}$ holds. Alternatively, time-variant solutions for ${}^G\boldsymbol{f}_d$ are not excluded.

Remark 3: Note that the actual target impedance behavior in (30) is not directly involved in the system control; rather, the proposed impedance control law (31) with Condition 1 provides an input for the control system (see Fig. 3). In principle, the proposed control law (31) differs from the target impedance law (30). However, as Theorem 1 shows, the target impedance behaviour (30) can be designed for (31) with $\mathbf{D}_d$ and $\mathbf{K}_d$ by using Condition 1.

Theorem 1 satisfies the first objective above: realization of the target impedance behaviour for the required Cartesian velocity vector $\dot{\boldsymbol{\chi}}_r$ in (19). The realization of the second objective (Object 2 qualifies as *virtually stable* in the sense of Definition 6) using the designed control laws (31)–(33) is analyzed next in Section V-A.

V. STABILITY ANALYSIS

The conceptual VPFs (see Definition 5) are a unique feature of VDC and they are used to address the dynamic interaction

between subsystems. The *virtual stability* (see Definition 6) of every subsystem ensures that, at every placed VCP, a negative VPF (at a driving VCP of a subsystem) is connected to its corresponding positive VPF (at a driven VCP of the adjacent subsystem). Thus, VPFs act as "stability connectors" between subsystems; eventually, they cancel each other out at every VCP [8]. Finally, as addressed in Theorem 2.1 in [8], the *virtual stability* of every subsystem ensures the L_2 and L_∞ stability (see Lemma 1) of the entire system.

As can be seen from Fig. 2, only one VCP (having a VPF $p_{\mathbf{T}_{O2}}$; see (28)) is specified for Object 2. However, in (28), there also exists another VPF $p_{\mathbf{G}}$ (characterizing the dynamic interaction between the manipulator and the environment), which has no "stabilizing counterpart". Consequently, it is control designer's obligation to ensure that a control is designed for the system such that Object 2 qualifies to be *virtually stable*. Next, in Section V-A, the VPF $p_{\mathbf{G}}$ between the manipulator and the environment is analyzed using Definitions 5–6, eventually leading to the stabilizing solution for $p_{\mathbf{G}}$ and *virtual stability* of Object 2. Finally, the stability of the entire system is proven in Section V-B.

A. Virtual Stability of Object 2

Using the designed control law (31), the following Lemma 5 can be derived.

Lemma 5: Definition 5, (14), (16), (19), (21), (30) and (31) yields

$$\begin{aligned} p_{\mathbf{G}} = &(\dot{\boldsymbol{\chi}}_d - \dot{\boldsymbol{\chi}})^T(\mathbf{D}_d\boldsymbol{\Lambda}_f\mathbf{D}_d - \mathbf{D}_d)(\dot{\boldsymbol{\chi}}_d - \dot{\boldsymbol{\chi}}) \\ &+ (\boldsymbol{\chi}_d - \boldsymbol{\chi})^T(\mathbf{K}_d\boldsymbol{\Lambda}_f\mathbf{K}_d - \boldsymbol{\Lambda}_\chi\mathbf{K}_d)(\boldsymbol{\chi}_d - \boldsymbol{\chi}) \\ &+ (\boldsymbol{\chi}_d - \boldsymbol{\chi})^T(2\mathbf{D}_d\boldsymbol{\Lambda}_f\mathbf{K}_d - \boldsymbol{\Lambda}_\chi\mathbf{D}_d - \mathbf{K}_d)(\dot{\boldsymbol{\chi}}_d - \dot{\boldsymbol{\chi}}). \end{aligned} \quad (34)$$

Proof: See Appendix B. ∎

Then, the following Lemma 6 is defined for $p_{\mathbf{G}}$ to provide sufficient conditions for the *virtual stability* of Object 2.

Lemma 6: Let the following constraints hold for the diagonal positive-definite matrices $\boldsymbol{\Lambda}_f$ and $\boldsymbol{\Lambda}_\chi$:

$$\boldsymbol{\Lambda}_f \geqslant \mathbf{D}_d^{-1} \quad (35)$$
$$\boldsymbol{\Lambda}_\chi \leqslant \mathbf{K}_d\boldsymbol{\Lambda}_f. \quad (36)$$

Then, it follows from Lemma 5 that

$$\int_0^t p_{\mathbf{G}}(\tau)d\tau \geqslant -\gamma_{\mathbf{G}} \quad (37)$$

holds with $0 \leqslant \gamma_{\mathbf{G}} < \infty$.

Proof: See Appendix C. ∎

Finally, the following Theorem 2 ensures that Object 2 qualifies as *virtually stable* in the sense of Definition 6.

Theorem 2: Let Condition 1 hold. Then, using Lemma 4, Lemma 5 and Lemma 6, Object 2 qualifies as *virtually stable* in the sense of Definition 6.

Proof: Let Condition 1 hold. Substituting $\mathbf{\Lambda}_f$ and $\mathbf{\Lambda}_\chi$ (in Condition 1) into Lemma 5 yields $p_{\mathbf{G}} = 0 \rightarrow \int_0^t p_{\mathbf{G}}(\tau)d\tau = 0$, which satisfies (37) in Lemma 6 (note that Condition 1 satisfies the constraints in (35) and (36) in Lemma 6). Consider the fact that Object 2 has one driven VCP associated with frame $\{\mathbf{T}_{\mathrm{O2}}\}$. Then, using Lemma 4 and (37), Object 2 qualifies as *virtually stable* in the sense of Definition 6. ∎

Remark 4: The design process for the proposed impedance control laws (31)–(33) is iterative. The *virtual stability*, i.e, Definition 6, of Object 2 determines the general constraints for this process. In addition, the designed control input should be written in the form of required velocity (see the footnote in Section IV-B2), constraining the design of (31). Then, given the target impedance law (30), Definition 5 is used to design the control laws (31)–(33), which realizes the Cartesian impedance behavior for the system (see Theorem 1) and provides *virtual stability* for Object 2 (see Theorem 2).

Remark 5: Assumption 1, Condition 1 and Theorem 1 define that $\mathbf{\Lambda}_f$ and $\mathbf{\Lambda}_\chi$ in (31) are not subject to unstable system behaviour. As the constraints (35) and (36) in Lemma 6 suggest, in addition to Condition 1, other stable solutions for $\mathbf{\Lambda}_f$ and $\mathbf{\Lambda}_\chi$ can also exist. This is true; a Z-width [41] can be determined for the impedance-controlled systems [42]. Note that selecting $\mathbf{\Lambda}_f$ and $\mathbf{\Lambda}_\chi$ with (35) and (36) (excluding solution in Condition 1) will result to different impedance behaviour in relation to the specified $\mathbf{D}_{\mathrm{d}}$ and $\mathbf{K}_{\mathrm{d}}$.

B. Stability of the Entire System

In relation to [23], only the control laws for Object 2 have been changed in this paper. Thus, in view of [23], the non-negative accompanying function and its time-derivative for the remaining subsystem, shown with dashed lines in Fig. 1(b)–(c), can be written as

$$\nu_{\mathbf{R}} \geqslant 0 \tag{38}$$

$$\dot{\nu}_{\mathbf{R}} \leqslant -p_{\mathbf{T}_{\mathrm{O2}}} \tag{39}$$

where $p_{\mathbf{T}_{\mathrm{O2}}}$ is the VPF at the driving VCP of this subsystem.

The following Theorem 3 guarantees the stability of the entire system, in view of Lemma 1.

Theorem 3: Consider Object 2, shown in Fig. 2 and described by Lemma 5. Furthermore, let the remaining subsystem be addressed with (38) and (39), and let Assumption 1 and Condition 1 hold. Then, using (27), (28), (38), (39) and Lemma 6, it can be shown that $^{\mathrm{O2}}V_{\mathrm{r}} - {}^{\mathrm{O2}}V \in L_2 \bigcap L_\infty$ holds, in view of Lemma 1. Consequently, this yields that $\mathbf{\Lambda}_f^{-1}(\dot{\boldsymbol{\chi}}_{\mathrm{d}} - \dot{\boldsymbol{\chi}}) + \mathbf{\Lambda}_f^{-1}\mathbf{\Lambda}_\chi(\boldsymbol{\chi}_{\mathrm{d}} - \boldsymbol{\chi}) + ({}^{\mathbf{G}}\boldsymbol{f}_{\mathrm{d}} - {}^{\mathbf{G}}\boldsymbol{f}) \in L_2 \bigcap L_\infty$ holds.

In the special case $({}^{\mathbf{G}}\boldsymbol{f}_{\mathrm{d}} - {}^{\mathbf{G}}\boldsymbol{f}) = 0$, it follows from Lemma 2 that $\dot{\boldsymbol{\chi}}_{\mathrm{d}} - \dot{\boldsymbol{\chi}} \in L_2 \bigcap L_\infty$ and $\boldsymbol{\chi}_{\mathrm{d}} - \boldsymbol{\chi} \in L_2 \bigcap L_\infty$ hold, with an asymptotic convergence for $\boldsymbol{\chi}_{\mathrm{d}} - \boldsymbol{\chi}$ (in the sense of Lemma 3).

Proof: See Appendix D. ∎

Remark 6: In Theorem 3, $({}^{\mathbf{G}}\boldsymbol{f}_{\mathrm{d}} - {}^{\mathbf{G}}\boldsymbol{f}) \neq 0$ denotes constrained motion and $({}^{\mathbf{G}}\boldsymbol{f}_{\mathrm{d}} - {}^{\mathbf{G}}\boldsymbol{f}) = 0$, with ${}^{\mathbf{G}}\boldsymbol{f}_{\mathrm{d}} = [0\ 0]^T$, denotes free-space motions.

VI. EXPERIMENTS

This section demonstrates the contact control performance of the proposed controller. System set-up and implementation issues are outlined in Section VI-A. Section VI-B demonstrates the controller's ability to prevent excessive contact forces when the manipulator collides with an object. The main results of this study are presented in Section VI-C, where the proposed control method is verified and the accuracy of Theorem 1 is shown in practice.

A. Experimental Set-up and Implementation Issues

The experimental set-up for the contact experiments is shown in Fig. 4. For the environmental contact, a set of wooden pallets was placed on a rubber mat. The set-up consisted of the following hardware components:

- dSpace DS1103 system, with 3 ms sample time
- 475 kg payload, denoted as M in Fig. 1(a)
- Bosch 4WRPEH10 proportional valve (100 dm³/min @ $\Delta\mathrm{p}$ = 3.5 MPa per notch) for cylinders
- Heidenhain ROD 456 incremental encoder (5000 inc/rev) with IVB interpolation units for joints 1 and 2, providing a theoretical piston position resolution < 1.2×10^{-3} mm
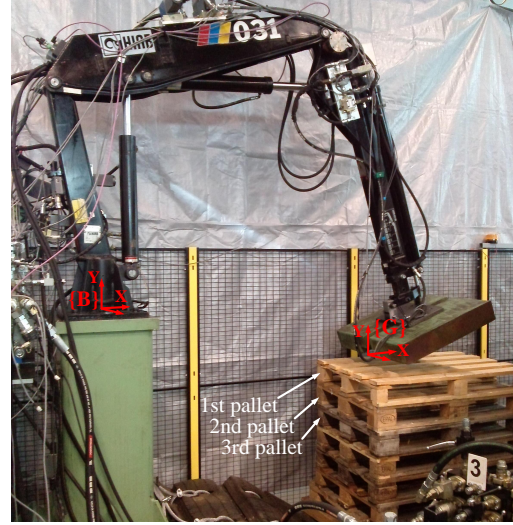- Druck PTX1400 pressure transmitters (range of 25 MPa)

Fig. 4. The experimental set-up. Manipulator's base frame $\{\mathbf{B}\}$ and end-effector target frame $\{\mathbf{G}\}$ are shown in red. The manipulator's position in this figure shows the starting point of the driven motion trajectories.

In the experiments, the manipulator should be stiff along the frame $\{\mathbf{G}\}$ X-axis (the direction of unconstrained motion) and compliant along the frame $\{\mathbf{G}\}$ Y-axis (the direction of constrained motion). For this reason, in $\mathbf{D}_{\mathrm{d}}$ and $\mathbf{K}_{\mathrm{d}}$, high gains were imposed along the X-axis and minor gains were imposed along the Y-axis. Table I shows $\mathbf{\Lambda}_f$ and $\mathbf{\Lambda}_\chi$ based on the determined $\mathbf{D}_{\mathrm{d}}$ and $\mathbf{K}_{\mathrm{d}}$.

TABLE I
GAINS FOR THE CARTESIAN CONTROL; SEE (31)

Specified $\mathbf{D}_{\mathrm{d}}$ and $\mathbf{K}_{\mathrm{d}}$ for the manipulator
$\mathbf{D}_{\mathrm{d}} = \mathrm{diag}(1 \cdot 10^5,\ 2.2 \cdot 10^3)$
$\mathbf{K}_{\mathrm{d}} = \mathrm{diag}(1 \cdot 10^6,\ 1.1 \cdot 10^4)$
$\Downarrow$
Condition 1
$\mathbf{\Lambda}_f = \mathrm{diag}(1.0 \cdot 10^{-5},\ 4.545 \cdot 10^{-4})$
$\mathbf{\Lambda}_\chi = \mathrm{diag}(10,\ 5)$

As Fig. 4 shows, a force sensor that measures the exact six-dimensional contact forces/moments at the end-effector was not used. The contact forces (applied by the manipulator on the environment) were estimated from the cylinder chamber pressures by removing the gravitational forces. This methodology to estimate the contact forces is discussed in more detail in [23]. Even though this method has some limitations, e.g., in force estimation accuracy, it may provide a practical solution for many heavy-duty operations where a fragile six-DOF force/moment sensor cannot be placed at the end-effector.

B. Collision Experiment

To test the proposed controller interaction dynamics behaviour, in the first set of experiments, a collision between the manipulator end-effector and an obstacle was arranged with three different Cartesian velocities. The manipulator position in Fig. 4 shows the starting point for the test trajectories. Then, a set of wooden pallets was placed in the way of the driven trajectories, so that the end-effector collided with the surface of the second pallet (when pallet 1 was removed); see Fig. 4. In the first trajectory, the end-effector was instructed to travel from -0.5 m to -1.0 m along the Y-axis of the system base frame $\{\mathbf{B}\}$ in one second. Then, the same path was driven over three seconds and, finally, over five seconds.

The plots in the first row of Fig. 5 show the manipulator position paths in blue, red and green, using a one-second trajectory, three-second trajectory and five-second trajectory, respectively. In these plots, the desired path is shown in black and the surface of the second pallet is depicted with a dashed line. As these plots show, the proposed controller limits the end-effector path when contact with the environment is established. The collision velocities between the end-effector and the environment were -0.52 m/s, -0.26 m/s and -0.18 m/s for the one-second trajectory, three-second trajectory and five-second trajectory, respectively. Note that the X-axes of the plots are scaled significantly smaller compared to the Y-axes.

The plot in the second row of Fig. 5 shows the measured end-effector contact forces in blue, red and green, using the one-second trajectory, three-second trajectory and five-second trajectory, respectively. The contact points are shown by blue circles. As this plot shows, the proposed controller efficiently limits the contact force (applied by the manipulator on the environment along the frame $\{\mathbf{G}\}$ Y-axis) to approximately -2800 N when contact with the environment is established. Because contact forces were estimated from the cylinder chamber pressures, inaccuracies exist in the estimates; therefore, the measured end-effector force before contact is not zero. This is due to the fact that system inertia and piston friction were not considered in the contact force estimation. Thus, the smaller velocity yields a better contact force estimation in free space. One practical method to estimate link accelerations (and to address the system inertia in the contact force estimation proposed in [23]) can be found in [43].

C. Target Impedance Behaviour

In the second set of experiments, three test cases were chosen to evaluate the ability of the proposed controller to
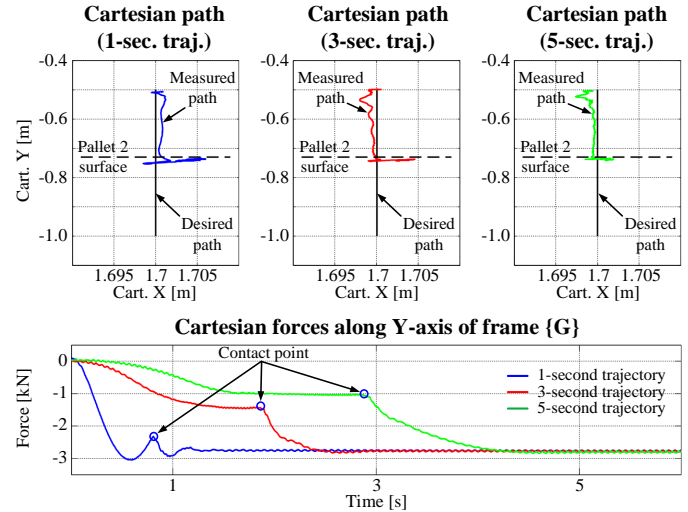

Fig. 5. The collision experiments. The plots in the first row show the measured end-effector paths in color, the desired paths in black and the surface of the environment with the dashed line. The test cases in the first row are driven using 1-second, 3-second and 5-second trajectories. The plot in the second row shows the measured contact forces in the test trajectories.

perform the target impedance behaviour. In test case 1, contact occurred on the surface of pallet 1. In test case 2, contact occurred on the surface of pallet 2 (after removing pallet 1). In test case 3, contact occurred on the surface of pallet 3 (after removing pallets 1 and 2). The manipulator position in Fig. 4 shows the starting point for the test trajectories.

Fig. 6 shows the test trajectory in the Cartesian coordinates (along the Y- and X-axes of the system base frame $\{\mathbf{B}\}$). The surfaces of wooden pallets 1–3 are marked in the first plot (see relation to Fig. 4). As Fig. 6 shows, the end-effector was first instructed to travel a distance of -0.5 m along the Y-axis in three seconds (see time interval 0–3 s from the first plot). Then, the end-effector was instructed to travel a distance of 0.5 m along the X-axis in three seconds (see time interval 3–6 s from the second plot). Finally, the end-effector was instructed to travel a distance of 0.5 m along the Y-axis in three seconds (see time interval 6–9 s from the first plot).

The main results of this paper are shown in Figs. 7–9. The first plots in Figs. 7–9 show the desired Cartesian paths in black and the measured Cartesian paths in red. The contact point is shown by a blue circle in these plots. As all these plots show, the proposed controller delimits the end-effector position when contact with the environment occurs, thus preventing excessive contact forces from being applied to the environment.
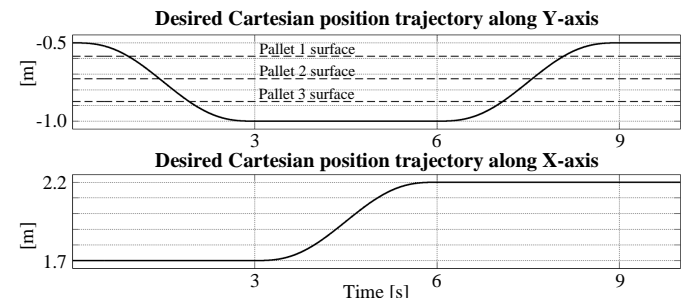

Fig. 6. Desired Cartesian position trajectories. The first plot shows the desired Cartesian position trajectory along the Y-axis, and the second plot shows the the desired Cartesian position trajectory along the X-axis. The surfaces of wooden pallets 1–3 are marked in the first plot (see the pallets in Fig. 4).

The second plots in Figs. 7–9 show the position tracking error along the X-axis of frame $\{\mathbf{G}\}$, in which direction the manipulator was made stiff. The contact point is shown by a blue circle in these plots. As these plots show, the maximum position tracking errors are all below 4 mm for the test trajectory. This can be considered a significant result in light of the manipulator scale, which has a reach of about 3.2 meters.

The last plots in Figs. 7–9 show the measured contact force exerted by the manipulator on the environment (shown in black) along the Y-axis of frame $\{\mathbf{G}\}$, in direction which the manipulator was made compliant. The contact point is shown by a blue circle in these plots. As addressed in Theorem 1, the target impedance behavior (30) should be achieved for the manipulator when the diagonal positive-definite matrices $\boldsymbol{\Lambda}_f$ and $\boldsymbol{\Lambda}_\chi$ in (31) are defined according to Condition 1. Consequently, the measured contact force should correspond to the contact force $^{\mathbf{G}}f_y$ solved from (30), i.e,[2]

$$^{\mathbf{G}}f_y = \mathbf{y}_f[\mathbf{D}_{\mathrm{d}}(\dot{\boldsymbol{\chi}}_{\mathrm{d}} - \dot{\boldsymbol{\chi}}) + \mathbf{K}_{\mathrm{d}}(\boldsymbol{\chi}_{\mathrm{d}} - \boldsymbol{\chi}) + {}^{\mathbf{G}}\boldsymbol{f}_{\mathrm{d}}] \qquad (40)$$

where $\mathbf{y}_f = [0\ 1]$, $^{\mathbf{G}}\boldsymbol{f}_{\mathrm{d}} = [0\ 0]^T$, and $(\dot{\boldsymbol{\chi}}_{\mathrm{d}} - \dot{\boldsymbol{\chi}})$ and $(\boldsymbol{\chi}_{\mathrm{d}} - \boldsymbol{\chi})$ are variables from the driven test cases. As the last plots in Figs. 7–9 show, the measured contact force (shown in black) corresponds accurately to the contact force suggested by (40) (shown in green). The nearly perfect matching of the two lines in these plots demonstrates the accuracy of Theorem 1. The maximum deviations between the measured contact force and (40) are 136 N, 170 N and 146 N in Figs. 7–9, respectively.

VII. CONCLUSIONS

In this paper, a novel impedance control method in the Cartesian space was developed for hydraulic manipulators. To acquire high-bandwidth closed-loop performance for the system, the internal control for the manipulator was designed according to the subsystem-dynamics-based virtual decomposition control (VDC) approach. Interaction dynamics between the hydraulic manipulator end-effector and the environment were analyzed in a novel manner, using the *virtual power flow*, which is a unique feature of VDC. From the analysis, an explicit method (see Condition 1) was developed to define parameters for the proposed impedance control law (external control for the manipulator), so that target impedance behavior can be designed for the hydraulic manipulator. The L_2 and L_∞ stability was guaranteed for both free-space and constrained motion control. The experimental results support the mathematical theorems on the stability-guaranteed (see Theorem 3) target impedance behaviour (see Theorem 1).

Even though a two-DOF system was studied in this paper, the developed approach is extendable to systems with any number of actuators. The results of this study can be used to realize compliant behaviour for complex and nonlinear systems, not limited only to hydraulic manipulators. The control method, which rigorously addresses the nonlinear dynamic behaviour of the system, can be applied to many dynamically challenging (robotic) tasks, such as legged locomotion.

---

[2]Note that (40) is solved from the target impedance law (30) by Hogan [25], which is not directly involved in the control laws; rather it is used to define $\boldsymbol{\Lambda}_f$ and $\boldsymbol{\Lambda}_\chi$ in control law (31); see Condition 1 and Remark 3.

Fig. 7. Test Case 1: Environmental contact on the surface of the first pallet (see Figs. 4 and 6). The collision velocity with pallet 1 was approx. -0.22 m/s. The first plot shows the desired Cartesian position path in black and the measured Cartesian path in red. The second plot shows the Cartesian position tracking along the frame $\{\mathbf{G}\}$ X-axis. The last plot shows the measured Cartesian contact force (along the frame $\{\mathbf{G}\}$ Y-axis) in black. The contact force suggested by the target impedance law (40) is shown in green.
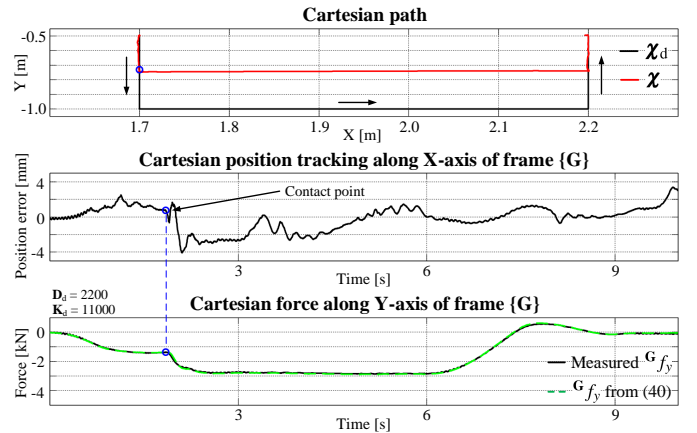
Fig. 8. Test Case 2: Environmental contact on the surface of the second pallet (see Figs. 4 and 6). The collision velocity with pallet 2 was approx. -0.27 m/s. The first plot shows the desired Cartesian position path in black and the measured Cartesian path in red. The second plot shows the Cartesian position tracking along the frame $\{\mathbf{G}\}$ X-axis. The last plot shows the measured Cartesian contact force (along the frame $\{\mathbf{G}\}$ Y-axis) in black. The contact force suggested by the target impedance law (40) is shown in green.
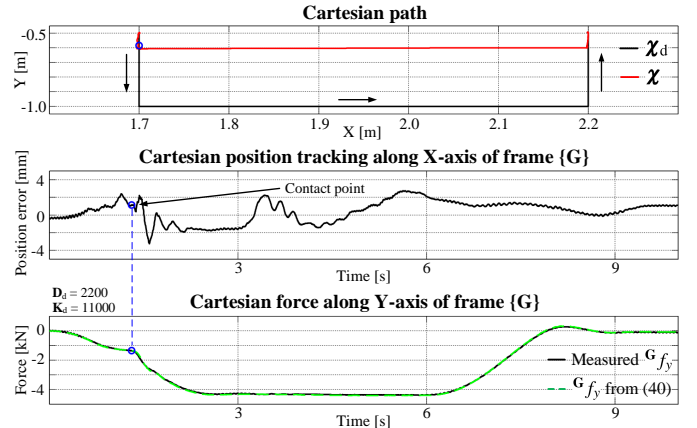

Fig. 9. Test Case 3: Environmental contact on the surface of the third pallet (see Figs. 4 and 6). The collision velocity with pallet 3 was approx. -0.28 m/s. The first plot shows the desired Cartesian position path in black and the measured Cartesian path in red. The second plot shows the Cartesian position tracking along the frame $\{\mathbf{G}\}$ X-axis. The last plot shows the measured Cartesian contact force (along the frame $\{\mathbf{G}\}$ Y-axis) in black. The contact force suggested by the target impedance law (40) is shown in green.
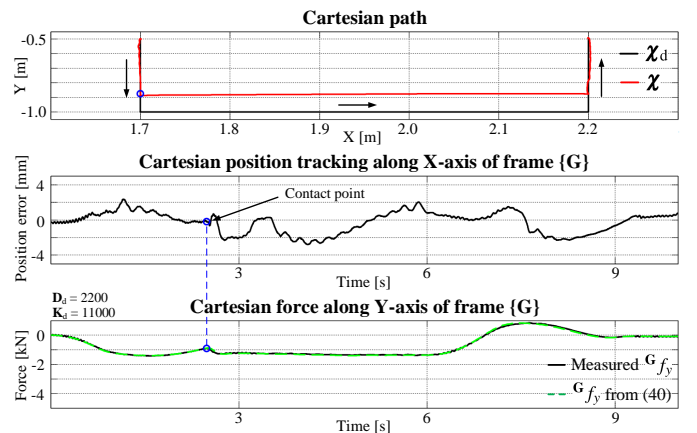
APPENDIX A
PROOF FOR THEOREM 1

Define $\mathbf{\Lambda}_f = \mathbf{D}_{\mathrm{d}}^{-1}$ and $\mathbf{\Lambda}_\chi = \mathbf{K}_{\mathrm{d}}\mathbf{\Lambda}_f$, as proposed in Condition 1. Then, it follows from the diagonal positive-definite property of $\mathbf{D}_{\mathrm{d}}$, $\mathbf{K}_{\mathrm{d}}$ and $\mathbf{\Lambda}_\chi$ that

$$\mathbf{D}_{\mathrm{d}}^{-1}\mathbf{\Lambda}_\chi\mathbf{D}_{\mathrm{d}} = \mathbf{\Lambda}_\chi \tag{41}$$

$$\mathbf{D}_{\mathrm{d}}\mathbf{K}_{\mathrm{d}}\mathbf{D}_{\mathrm{d}}^{-1} = \mathbf{K}_{\mathrm{d}} \tag{42}$$

hold. Substituting (30) into (31) and using Condition 1 and (41) yields

$$\begin{aligned}
\dot{\boldsymbol{\chi}}_{\mathrm{r}} &= \dot{\boldsymbol{\chi}}_{\mathrm{d}} + \mathbf{\Lambda}_\chi(\boldsymbol{\chi}_{\mathrm{d}} - \boldsymbol{\chi}) - \mathbf{\Lambda}_f[\mathbf{D}_{\mathrm{d}}(\dot{\boldsymbol{\chi}}_{\mathrm{d}} - \dot{\boldsymbol{\chi}}) + \mathbf{K}_{\mathrm{d}}(\boldsymbol{\chi}_{\mathrm{d}} - \boldsymbol{\chi})] \\
&= \dot{\boldsymbol{\chi}}_{\mathrm{d}} + \mathbf{\Lambda}_\chi(\boldsymbol{\chi}_{\mathrm{d}} - \boldsymbol{\chi}) - \mathbf{D}_{\mathrm{d}}^{-1}\mathbf{D}_{\mathrm{d}}(\dot{\boldsymbol{\chi}}_{\mathrm{d}} - \dot{\boldsymbol{\chi}}) \\
&\quad - \mathbf{D}_{\mathrm{d}}^{-1}\mathbf{\Lambda}_\chi\mathbf{D}_{\mathrm{d}}(\boldsymbol{\chi}_{\mathrm{d}} - \boldsymbol{\chi}) \\
&= \dot{\boldsymbol{\chi}}_{\mathrm{d}} + \mathbf{\Lambda}_\chi(\boldsymbol{\chi}_{\mathrm{d}} - \boldsymbol{\chi}) - \dot{\boldsymbol{\chi}}_{\mathrm{d}} + \dot{\boldsymbol{\chi}} - \mathbf{\Lambda}_\chi(\boldsymbol{\chi}_{\mathrm{d}} - \boldsymbol{\chi}) \\
&= \dot{\boldsymbol{\chi}}.
\end{aligned} \tag{43}$$

Then, using Condition 1, (42) and (43) yields

$$\begin{aligned}
&\dot{\boldsymbol{\chi}}_{\mathrm{r}} = \dot{\boldsymbol{\chi}}_{\mathrm{d}} + \mathbf{\Lambda}_\chi(\boldsymbol{\chi}_{\mathrm{d}} - \boldsymbol{\chi}) + \mathbf{\Lambda}_f({}^{\mathbf{G}}\boldsymbol{f}_{\mathrm{d}} - {}^{\mathbf{G}}\boldsymbol{f}) \\
\Leftrightarrow\ &{}^{\mathbf{G}}\boldsymbol{f}_{\mathrm{d}} - {}^{\mathbf{G}}\boldsymbol{f} = -\mathbf{\Lambda}_f^{-1}(\dot{\boldsymbol{\chi}}_{\mathrm{d}} - \dot{\boldsymbol{\chi}}_{\mathrm{r}}) - \mathbf{\Lambda}_f^{-1}\mathbf{\Lambda}_\chi(\boldsymbol{\chi}_{\mathrm{d}} - \boldsymbol{\chi}) \\
\Leftrightarrow\ &{}^{\mathbf{G}}\boldsymbol{f}_{\mathrm{d}} - {}^{\mathbf{G}}\boldsymbol{f} = -\mathbf{D}_{\mathrm{d}}(\dot{\boldsymbol{\chi}}_{\mathrm{d}} - \dot{\boldsymbol{\chi}}) - \mathbf{D}_{\mathrm{d}}\mathbf{K}_{\mathrm{d}}\mathbf{D}_{\mathrm{d}}^{-1}(\boldsymbol{\chi}_{\mathrm{d}} - \boldsymbol{\chi}) \\
\Leftrightarrow\ &{}^{\mathbf{G}}\boldsymbol{f}_{\mathrm{d}} - {}^{\mathbf{G}}\boldsymbol{f} = -\mathbf{D}_{\mathrm{d}}(\dot{\boldsymbol{\chi}}_{\mathrm{d}} - \dot{\boldsymbol{\chi}}) - \mathbf{K}_{\mathrm{d}}(\boldsymbol{\chi}_{\mathrm{d}} - \boldsymbol{\chi}).
\end{aligned} \tag{44}$$

Note that the first row in (44) is equal to (31), whereas the last row is equal to (30). This completes the proof for Theorem 1. ∎

APPENDIX B
PROOF FOR LEMMA 5

It follows from Definition 5, (14), (16), (19), (21), (30), (31), $\mathbf{N}_{\mathrm{c}}^T\mathbf{N}_{\mathrm{c}} = \mathbf{I}_{2\times2}$ and the diagonal positive-definite property[3] of matrices $\mathbf{\Lambda}_\chi$, $\mathbf{\Lambda}_f$, $\mathbf{D}_{\mathrm{d}}$ and $\mathbf{K}_{\mathrm{d}}$ that

$$\begin{aligned}
p_{\mathbf{G}} &= ({}^{\mathbf{G}}V_{\mathrm{r}} - {}^{\mathbf{G}}V)^T({}^{\mathbf{G}}F_{\mathrm{r}} - {}^{\mathbf{G}}F) \\
&= [(\dot{\boldsymbol{\chi}}_{\mathrm{d}} - \dot{\boldsymbol{\chi}}) + \mathbf{\Lambda}_\chi(\boldsymbol{\chi}_{\mathrm{d}} - \boldsymbol{\chi}) + \mathbf{\Lambda}_f({}^{\mathbf{G}}\boldsymbol{f}_{\mathrm{d}} - {}^{\mathbf{G}}\boldsymbol{f})]^T\mathbf{N}_{\mathrm{c}}^T \\
&\quad \times \mathbf{N}_{\mathrm{c}}({}^{\mathbf{G}}\boldsymbol{f}_{\mathrm{d}} - {}^{\mathbf{G}}\boldsymbol{f}) \\
&= (\dot{\boldsymbol{\chi}}_{\mathrm{d}} - \dot{\boldsymbol{\chi}})^T({}^{\mathbf{G}}\boldsymbol{f}_{\mathrm{d}} - {}^{\mathbf{G}}\boldsymbol{f}) + (\boldsymbol{\chi}_{\mathrm{d}} - \boldsymbol{\chi})^T\mathbf{\Lambda}_\chi^T({}^{\mathbf{G}}\boldsymbol{f}_{\mathrm{d}} - {}^{\mathbf{G}}\boldsymbol{f}) \\
&\quad + ({}^{\mathbf{G}}\boldsymbol{f}_{\mathrm{d}} - {}^{\mathbf{G}}\boldsymbol{f})^T\mathbf{\Lambda}_f^T({}^{\mathbf{G}}\boldsymbol{f}_{\mathrm{d}} - {}^{\mathbf{G}}\boldsymbol{f}) \\
&= -(\dot{\boldsymbol{\chi}}_{\mathrm{d}} - \dot{\boldsymbol{\chi}})^T[\mathbf{D}_{\mathrm{d}}(\dot{\boldsymbol{\chi}}_{\mathrm{d}} - \dot{\boldsymbol{\chi}}) + \mathbf{K}_{\mathrm{d}}(\boldsymbol{\chi}_{\mathrm{d}} - \boldsymbol{\chi})] \\
&\quad - (\boldsymbol{\chi}_{\mathrm{d}} - \boldsymbol{\chi})^T\mathbf{\Lambda}_\chi^T[\mathbf{D}_{\mathrm{d}}(\dot{\boldsymbol{\chi}}_{\mathrm{d}} - \dot{\boldsymbol{\chi}}) + \mathbf{K}_{\mathrm{d}}(\boldsymbol{\chi}_{\mathrm{d}} - \boldsymbol{\chi})] \\
&\quad + [\mathbf{D}_{\mathrm{d}}(\dot{\boldsymbol{\chi}}_{\mathrm{d}} - \dot{\boldsymbol{\chi}}) + \mathbf{K}_{\mathrm{d}}(\boldsymbol{\chi}_{\mathrm{d}} - \boldsymbol{\chi})]^T\mathbf{\Lambda}_f^T \\
&\quad \times [\mathbf{D}_{\mathrm{d}}(\dot{\boldsymbol{\chi}}_{\mathrm{d}} - \dot{\boldsymbol{\chi}}) + \mathbf{K}_{\mathrm{d}}(\boldsymbol{\chi}_{\mathrm{d}} - \boldsymbol{\chi})] \\
&= (\dot{\boldsymbol{\chi}}_{\mathrm{d}} - \dot{\boldsymbol{\chi}})^T(\mathbf{D}_{\mathrm{d}}\mathbf{\Lambda}_f\mathbf{D}_{\mathrm{d}} - \mathbf{D}_{\mathrm{d}})(\dot{\boldsymbol{\chi}}_{\mathrm{d}} - \dot{\boldsymbol{\chi}}) \\
&\quad + (\boldsymbol{\chi}_{\mathrm{d}} - \boldsymbol{\chi})^T(\mathbf{K}_{\mathrm{d}}\mathbf{\Lambda}_f\mathbf{K}_{\mathrm{d}} - \mathbf{\Lambda}_\chi\mathbf{K}_{\mathrm{d}})(\boldsymbol{\chi}_{\mathrm{d}} - \boldsymbol{\chi}) \\
&\quad + (\boldsymbol{\chi}_{\mathrm{d}} - \boldsymbol{\chi})^T(2\mathbf{D}_{\mathrm{d}}\mathbf{\Lambda}_f\mathbf{K}_{\mathrm{d}} - \mathbf{\Lambda}_\chi\mathbf{D}_{\mathrm{d}} - \mathbf{K}_{\mathrm{d}})(\dot{\boldsymbol{\chi}}_{\mathrm{d}} - \dot{\boldsymbol{\chi}})
\end{aligned} \tag{45}$$

holds, which validates Lemma 5. ∎

[3]The diagonal property of matrices $\mathbf{\Lambda}_\chi$, $\mathbf{\Lambda}_f$, $\mathbf{D}_{\mathrm{d}}$ and $\mathbf{K}_{\mathrm{d}}$ yields $\mathbf{\Lambda}_\chi^T = \mathbf{\Lambda}_\chi$, $\mathbf{\Lambda}_f^T = \mathbf{\Lambda}_f$, $\mathbf{D}_{\mathrm{d}}^T = \mathbf{D}_{\mathrm{d}}$ and $\mathbf{K}_{\mathrm{d}}^T = \mathbf{K}_{\mathrm{d}}$.

APPENDIX C
PROOF FOR LEMMA 6

Let $\mathbf{\Lambda}_f \geqslant \mathbf{D}_{\mathrm{d}}^{-1}$ and $\mathbf{\Lambda}_\chi \leqslant \mathbf{K}_{\mathrm{d}}\mathbf{\Lambda}_f$ hold, as defined in (35) and (36). Then, it follows from (45) that

$$p_{\mathbf{G}} \geqslant (\boldsymbol{\chi}_{\mathrm{d}} - \boldsymbol{\chi})^T\mathbf{A}_1(\dot{\boldsymbol{\chi}}_{\mathrm{d}} - \dot{\boldsymbol{\chi}}) \tag{46}$$

holds, where $\mathbf{A}_1 = (2\mathbf{D}_{\mathrm{d}}\mathbf{\Lambda}_f\mathbf{K}_{\mathrm{d}} - \mathbf{\Lambda}_\chi\mathbf{D}_{\mathrm{d}} - \mathbf{K}_{\mathrm{d}}) \geqslant 0$ holds, in view of (35) and (36).

Integrating (46) over time yields that

$$\begin{aligned}
\int_0^t p_{\mathbf{G}}(\tau)d\tau &\geqslant \frac{1}{2}(\boldsymbol{\chi}_{\mathrm{d}}(t) - \boldsymbol{\chi}(t))^T\mathbf{A}_1(\boldsymbol{\chi}_{\mathrm{d}}(t) - \boldsymbol{\chi}(t)) \\
&\quad - \frac{1}{2}(\boldsymbol{\chi}_{\mathrm{d}}(0) - \boldsymbol{\chi}(0))^T\mathbf{A}_1(\boldsymbol{\chi}_{\mathrm{d}}(0) - \boldsymbol{\chi}(0)) \\
&\geqslant -\frac{1}{2}(\boldsymbol{\chi}_{\mathrm{d}}(0) - \boldsymbol{\chi}(0))^T\mathbf{A}_1(\boldsymbol{\chi}_{\mathrm{d}}(0) - \boldsymbol{\chi}(0)) \\
&= -\gamma_{\mathbf{G}}
\end{aligned} \tag{47}$$

holds with $0 \leqslant \gamma_{\mathbf{G}} < \infty$, which validates Lemma 6. ∎

APPENDIX D
PROOF FOR THEOREM 3

Let the remaining subsystem, shown with dashed lines in Fig. 1(b)–(c), be addressed with (38) and (39), and let Assumption 1 and Condition 1 hold. Then, in view of (27) and (38), the non-negative accompanying function v_{tot} for the entire manipulator can be chosen as

$$\begin{aligned}
v_{\mathrm{tot}} &= v_{\mathbf{R}} + v_{\mathbf{O}_2} \\
&\geqslant \frac{1}{2}({}^{\mathbf{O}_2}V_{\mathrm{r}} - {}^{\mathbf{O}_2}V)^T\mathbf{M}_{\mathbf{O}_2}({}^{\mathbf{O}_2}V_{\mathrm{r}} - {}^{\mathbf{O}_2}V) \\
&\quad + \frac{1}{2}\sum_{i=1}^{13}\frac{(\theta_{\mathbf{O}_2 i} - \widehat{\theta}_{\mathbf{O}_2 i})^2}{\rho_{\mathbf{O}_2 i}}.
\end{aligned} \tag{48}$$

Then, in view of (28) and (39), the time derivative of (48) can be written as

$$\begin{aligned}
\dot{v}_{\mathrm{tot}} &\leqslant -({}^{\mathbf{O}_2}V_{\mathrm{r}} - {}^{\mathbf{O}_2}V)^T\mathbf{K}_{\mathbf{O}_2}({}^{\mathbf{O}_2}V_{\mathrm{r}} - {}^{\mathbf{O}_2}V) - p_{\mathbf{T}_{\mathbf{O}2}} + p_{\mathbf{T}_{\mathbf{O}2}} - p_{\mathbf{G}} \\
&= -({}^{\mathbf{O}_2}V_{\mathrm{r}} - {}^{\mathbf{O}_2}V)^T\mathbf{K}_{\mathbf{O}_2}({}^{\mathbf{O}_2}V_{\mathrm{r}} - {}^{\mathbf{O}_2}V) - p_{\mathbf{G}}
\end{aligned} \tag{49}$$

where, in view of Lemma 6,

$$\int_0^t p_{\mathbf{G}}(\tau)d\tau \geqslant -\gamma_{\mathbf{G}} \tag{50}$$

holds with $0 \leqslant \gamma_{\mathbf{G}} < \infty$.

It follows directly from Lemma 1 and (48)–(50) that

$$^{\mathbf{O}_2}V_{\mathrm{r}} - {}^{\mathbf{O}_2}V \in L_2\bigcap L_\infty \tag{51}$$

holds. Using (14), (15), (19), (20) and (51) yields

$$\dot{\boldsymbol{\chi}}_{\mathrm{r}} - \dot{\boldsymbol{\chi}} \in L_2\bigcap L_\infty. \tag{52}$$

Then, subtracting $\dot{\boldsymbol{\chi}}$ from both sides of (31) and using (52) yields

$$\mathbf{\Lambda}_f^{-1}(\dot{\boldsymbol{\chi}}_{\mathrm{d}} - \dot{\boldsymbol{\chi}}) + \mathbf{\Lambda}_f^{-1}\mathbf{\Lambda}_\chi(\boldsymbol{\chi}_{\mathrm{d}} - \boldsymbol{\chi}) + ({}^{\mathbf{G}}\boldsymbol{f}_{\mathrm{d}} - {}^{\mathbf{G}}\boldsymbol{f}) \in L_2\bigcap L_\infty. \tag{53}$$

Let $({}^{\mathbf{G}}\boldsymbol{f}_{\mathrm{d}} - {}^{\mathbf{G}}\boldsymbol{f}) = 0$ hold. Subtracting $\dot{\boldsymbol{\chi}}$ from both sides of (31) yields

$$\dot{\boldsymbol{\chi}}_{\mathrm{r}} - \dot{\boldsymbol{\chi}} = (\dot{\boldsymbol{\chi}}_{\mathrm{d}} - \dot{\boldsymbol{\chi}}) + \mathbf{\Lambda}_\chi(\boldsymbol{\chi}_{\mathrm{d}} - \boldsymbol{\chi}). \tag{54}$$

Then, it follows directly from Lemma 2, (52) and (54) that

$$\dot{\boldsymbol{\chi}}_{\mathrm{d}} - \dot{\boldsymbol{\chi}} \in L_2 \bigcap L_\infty \tag{55}$$

$$\boldsymbol{\chi}_{\mathrm{d}} - \boldsymbol{\chi} \in L_2 \bigcap L_\infty \tag{56}$$

hold. Then, Lemma 3 yields $\lim_{t \to \infty} \left[\boldsymbol{\chi}_{\mathrm{d}}(t) - \boldsymbol{\chi}(t) \right] = 0.$ ∎

REFERENCES

[1] A. Alleyne and R. Liu, "On the limitations of force tracking control for hydraulic servosystems," *J. Dyn. Syst.–T. ASME*, vol. 121, no. 2, pp. 184–190, 1999.

[2] C. An and J. Hollerbach, "Dynamic stability issues in force control of manipulators," in *Proc. American Control Conf.*, 1987, pp. 821–827.

[3] ——, "Kinematic stability issues in force control of manipulators," in *Proc. IEEE Int. Conf. Robotics and Autom.*, vol. 4, 1987, pp. 897–903.

[4] ——, "The role of dynamic models in cartesian force control of manipulators," *Int. J. Robot. Res.*, vol. 8, no. 4, pp. 51–72, 1989.

[5] S. Eppinger and W. Seering, "Understanding bandwidth limitations in robot force control," in *Proc. IEEE Int. Conf. Robotics and Autom.*, vol. 4, 1987, pp. 904–909.

[6] ——, "Three dynamic problems in robot force control," in *Proc. IEEE Int. Conf. Robotics and Autom.*, 1989, pp. 392–397.

[7] T. Yoshikawa, "Force control of robot manipulators," in *Proc. IEEE Int. Conf. Robotics and Autom.*, vol. 1, Apr. 2000, pp. 220–226.

[8] W.-H. Zhu, *Virtual Decomposition Control - Toward Hyper Degrees of Freedom Robots*. Springer-Verlag, 2010.

[9] C. An, C. Atkeson, and J. Hollerbach, *Model-based control of a robot manipulator*. MIT press Cambridge, MA, 1988, vol. 214.

[10] L. Sciavicco and B. Siciliano, *Modeling and Control of Robot Manipulators*. London: Springer, 2000.

[11] R. N. Jazar, *Theory of applied robotics: kinematics, dynamics, and control*. Springer Science & Business Media, 2010.

[12] W.-H. Zhu *et al.*, "Virtual decomposition based control for generalized high dimensional robotic systems with complicated structure," *IEEE Trans. Robot. Autom.*, vol. 13, no. 3, pp. 411–436, 1997.

[13] W.-H. Zhu, Z. Bien, and J. De Schutter, "Adaptive motion/force control of multiple manipulators with joint flexibility based on virtual decomposition," *IEEE Trans. Autom. Control*, vol. 43, no. 1, pp. 46–60, 1998.

[14] W.-H. Zhu and J. De Schutter, "Adaptive control of mixed rigid/flexible joint robot manipulators based on virtual decomposition," *IEEE Trans. Robot. Autom.*, vol. 15, no. 2, pp. 310–317, 1999.

[15] ——, "Control of two industrial manipulators rigidly holding an egg," *IEEE Control Systems*, vol. 19, no. 2, pp. 24–30, 1999.

[16] ——, "Experimental verifications of virtual-decomposition-based motion/force control," *IEEE Trans. Robot. Autom.*, vol. 18, no. 3, pp. 379–386, 2002.

[17] W.-H. Zhu and G. Vukovich, "Virtual decomposition control for modular robot manipulators," in *Proc. IFAC World Congress*, Sep. 2011, pp. 13 486–13 491.

[18] W.-H. Zhu *et al.*, "Precision control of modular robot manipulators: The VDC approach with embedded FPGA," *IEEE Trans. Robot.*, vol. 29, no. 5, pp. 1162–1179, 2013.

[19] W.-H. Zhu and J. Piedboeuf, "Adaptive output force tracking control of hydraulic cylinders with applications to robot manipulators," *J. Dynamic Syst., Meas. Control*, vol. 127, no. 2, pp. 206–217, Jun. 2005.

[20] J. Koivumäki and J. Mattila, "The automation of multi degree of freedom hydraulic crane by using virtual decomposition control," in *Proc. IEEE/ASME Int. Conf. Adv. Intell. Mechatr.*, 2013, pp. 912–919.

[21] ——, "An energy-efficient high performance motion control of a hydraulic crane applying virtual decomposition control," in *Proc. IEEE/RJS Int. Conf. Intell. Robots Syst.*, 2013, pp. 4426–4433.

[22] ——, "High performance non-linear motion/force controller design for redundant hydraulic construction crane automation," *Automation in Construction*, vol. 51, pp. 59–77, 2015.

[23] ——, "Stability-guaranteed force-sensorless contact force/motion control of heavy-duty hydraulic manipulators," *IEEE Trans. Robot.*, vol. 31, no. 4, 2015.

[24] M. Raibert and J. Craig, "Hybrid position/force control of manipulators," *J. Dyn. Syst.–T. ASME*, vol. 103, no. 2, pp. 126–133, 1981.

[25] N. Hogan, "Impedance control: An approach to manipulation: Parts I-III," *J. Dyn. Syst.–T. ASME*, vol. 107, no. 1, pp. 1–24, 1985.

[26] D. Whitney, "Historical perspective and state of the art in robot force control," in *Proc. IEEE Int. Conf. Robotics and Autom.*, vol. 2, 1985, pp. 262–268.

[27] M. Vukobratović and A. Tuneski, "Contact control concepts in manipulation robotics – an overview," *IEEE Trans. Ind. Electron.*, vol. 41, no. 1, pp. 12–24, Feb. 1994.

[28] O. Khatib, "A unified approach for motion and force control of robot manipulators: The operational space formulation," *IEEE Trans. Robot. Autom.*, vol. 3, no. 1, pp. 43–53, 1987.

[29] J. De Schutter and H. Van Brussel, "Compliant robot motion: Parts I-II," *Int. J. Robot. Res.*, vol. 7, no. 4, pp. 3–17, 1988.

[30] N. McClamroch and D. Wang, "Feedback stabilization and tracking of constrained robots," *IEEE Trans. Autom. Control*, vol. 33, no. 5, pp. 419–426, 1988.

[31] S. Chiaverini and L. Sciavicco, "The parallel approach to force/position control of robotic manipulators," *IEEE Trans. Robot. Autom.*, vol. 9, no. 4, pp. 361–373, 1993.

[32] J. Pratt *et al.*, "Virtual model control: An intuitive approach for bipedal locomotion," *Int. J. Robot. Res.*, vol. 20, no. 2, pp. 129–143, 2001.

[33] B. Heinrichs, N. Sepehri, and A. Thornton-Trump, "Position-based impedance control of an industrial hydraulic manipulator," *IEEE Control Systems*, vol. 17, no. 1, pp. 46–52, 1997.

[34] S. Tafazoli *et al.*, "Impedance control of a teleoperated excavator," *IEEE Trans. Control Syst. Technol.*, vol. 10, no. 3, pp. 355–367, 2002.

[35] S. Salcudean, S. Tafazoli, P. Lawrence, and I. Chau, "Impedance control of a teleoperated mini excavator," in *Proc. 8th Int. IEEE Conf. on Advanced Robotics*, 1997, pp. 19–25.

[36] S. Salcudean *et al.*, "Bilateral matched-impedance teleoperation with application to excavator control," *IEEE Control Systems*, vol. 19, no. 6, pp. 29–37, 1999.

[37] H. Zeng and N. Sepehri, "On tracking control of cooperative hydraulic manipulators," *Int. J. Control*, vol. 80, no. 3, pp. 454–469, 2007.

[38] H. Zeng, "Nonlinear control of co-operating hydraulic manipulators," Ph.D. dissertation, University of Manitoba, 2007.

[39] C. Semini *et al.*, "Towards versatile legged robots through active impedance control," *Int. J. Robot. Res.*, vol. 34, no. 7, pp. 1003–1020, 2015.

[40] G. Tao, "A simple alternative to the barbalat lemma," *IEEE Trans. Autom. Control*, vol. 42, no. 5, p. 698, may 1997.

[41] J. Colgate and J. Brown, "Factors affecting the z-width of a haptic display," in *Proc. IEEE Int. Conf. Robotics and Automation*, 1994, pp. 3205–3210.

[42] T. Boaventura *et al.*, "Stability and performance of the compliance controller of the quadruped robot HyQ," in *Proc. of IEEE/RSJ Int. Conf. on Intel. Robots and Syst.*, 2013, pp. 1458–1464.

[43] J. Vihonen, J. Honkakorpi, J. Tuominen, J. Mattila, and A. Visa, "Linear accelerometers and rate gyros for rotary joint angle estimation of heavy-duty mobile manipulators using forward kinematic modeling," *IEEE/ASME Trans. Mechatronics*, vol. 21, no. 3, pp. 1765–1774, 2016.

Janne Koivumäki received his M.Sc. degree in Automation Engineering from the Tampere University of Technology (TUT), Finland, in 2012. He has worked at IHA, TUT, since 2011 and is currently pursuing a doctoral degree in Machine Automation. From 1/2015 his work has been supported by the Academy of Finland under the project "Cooperative heavy-duty hydraulic manipulators for sustainable subsea infrastructure installation and dismantling". His research interests include a control of electro-hydraulic systems and hydraulic robotic manipulators, nonlinear model-based control, contact force/motion control and energy-efficiency of fluid power systems.

Jouni Mattila received his M.Sc. (Eng.) in 1995 and Dr. Tech. in 2000, both from the Tampere University of Technology (TUT), Finland. He has been involved in numerous industrial research projects, including the Sandvik AutoMine® with Hermia Group Ltd. He is currently a Professor in Machine Automation in the Dept. of Intelligent Hydraulics and Automation (IHA), TUT. For the past ten years, he has been a program manager on ITER fusion reactor maintenance projects involving research on heavy-duty hydraulic robotic manipulators. His research interests include machine automation, nonlinear model-based control of hydraulic robotic manipulators and energy-efficiency of fluid power systems.